Medical Image Analysis 53 (2019) 95–103

Contents lists available at ScienceDirect

Medical Image Analysis

journal homepage: www.elsevier.com/locate/media

Novel and facile criterion to assess the accuracy of WSS estimation by 4D flow MRI

Seungbin Ko[a,1], Byungkuen Yang[a,1], Jee-Hyun Cho[b], Jeesoo Lee[a,c,*], Simon Song[a,c,*]

[a] Department of Mechanical Engineering, Hanyang University, Seoul, 04763, South Korea
[b] Bioimaging Research Team, Korea Basic Science Institute, Cheongju, 28119, South Korea
[c] Institute of Nano Science and Technology, Hanyang University, Seoul, 04763, South Korea

ARTICLE INFO

Article history:
Received 11 June 2018
Revised 15 January 2019
Accepted 26 January 2019
Available online 31 January 2019

Keywords:
Wall shear stress
Reynolds resolution
Accuracy
4D flow MRI

ABSTRACT

Four-dimensional flow magnetic resonance imaging (4D flow MRI) is a versatile tool to obtain hemodynamic information and anatomic information simultaneously. The wall shear stress (WSS), a force exerted on a vessel wall in parallel, is one of the hemodynamic parameters available with 4D flow MRI and is thought to play an important role in clinical applications such as assessing the development of atherosclerosis. Nevertheless, the accuracy of WSS obtained with 4D flow MRI is rarely evaluated or reported in literature, especially in the in vivo studies. We propose a novel and facile criterion called Reynolds resolution to assess the accuracy of WSS estimation in 4D flow MRI studies. Reynolds resolution consists of a spatial resolution, encoding velocity, kinematic viscosity of a working fluid, and signal-to-noise ratio, which are readily accessible information in 4D flow MRI measurements. We explored the relationship between Reynolds resolution and the WSS error. To include diverse and extensive cases, we measured three circular tubing flows with a diameter of 40, 8, and 2 mm. The 40 mm tubing flow was measured by 3 Tesla (T) human MR scanner with a knee coil and spatial resolution of 0.5 mm. The 8 and 2 mm tubing flows were both measured by 4.7 T MR scanner, but the scans were performed with a conventional birdcage coil (8 mm tubing) and a custom-made solenoid coil (2 mm tubing), respectively. The spatial resolution was varied from 0.2, 0.4 or 0.8 mm for the 8 mm tubing flow, but was fixed at 0.090 mm for 2 mm tubing flow. In addition, the near-wall velocity gradient, required to be determined prior to the WSS, was calculated using two methods; these included assuming a linear velocity profile or quadratic velocity profile near wall. The accuracy of WSS obtained using each method and tubing flow was evaluated against the theoretical WSS value. As a result, we found that Reynolds resolution is in logarithmic relation to the WSS error.

1. Introduction

Cardiovascular disease (CVD) is known to have the highest mortality rate according to a recent report (Kochanek et al., 2016). In order to understand CVD, the hemodynamics of a cardiovascular flow needs to be investigated because a fluid flow plays a dominant role in a cardiovascular system. The phase-contrast magnetic resonance imaging (MRI) technique is an effective clinical modality that can obtain vast quantities of information of both cardiovascular flow and anatomy simultaneously. The three-dimensional (3D) cine (time-resolved) phase-contrast cardiovascular magnetic resonance (CMR) with three-directional velocity-encoding is called 4D flow MRI (Dyverfeldt et al., 2015). Recent advances in 4D flow MRI have enabled the measurement of a complete and quantitative velocity vector field of a blood flow and relate the cardiovascular disease to hemodynamic parameters (Cebral et al., 2009; Pantos et al., 2007; Strecker et al., 2012; van Ooij et al., 2017). For example, several researchers have utilized 4D flow MRI and identified hemodynamic features with a simple analysis of the velocity vector field or a streamline pattern or a complex evaluation of fluid dynamic parameters such as wall shear stress (WSS) (Calkoen et al., 2015; Morbiducci et al., 2009; She et al., 2017), oscillatory shear index (OSI) (Harloff et al., 2010; Markl et al., 2013; Tsuji et al., 2002), turbulent kinetic energy (Dyverfeldt et al., 2013; Ha et al., 2016a), and pressure field (Donati et al., 2015; Ebbers et al., 2001). Among these parameters, the WSS, that is a direct measure of the shear

* Corresponding authors at: Department of Mechanical Engineering, Hanyang University, 222 Wangsimni-Ro, Seongdong-Gu, Seoul, 04763, South Korea.
E-mail addresses: jeesoolee@hanyang.ac.kr (J. Lee), simonsong@hanyang.ac.kr (S. Song).
[1] These authors equally contributed to this work.

https://doi.org/10.1016/j.media.2019.01.009
1361-8415/

force acting on a vessel wall in parallel, is considered as one of the key factors that causes atherosclerosis and affects the endothelial cell dysfunction (Cecchi et al., 2011; Malek et al., 1999; Reneman et al., 2006; Wahle et al., 2006).

Numerous studies to determine WSS from 4D flow MRI velocity data obtained at the cross section of a blood vessel have been actively performed since the early 2000s. Many studies used an interpolation method to smoothen and make the measured velocity data differentiable near the wall (Bürk et al., 2012; Hope et al., 2013; Kolipaka et al., 2017; Markl et al., 2010; Meierhofer et al., 2013). A method of finite-element interpolation on a velocity field was also reported (Montalba et al., 2018; Sotelo et al., 2016). Recent advances in MRI hardware and software enabled the evaluation of the WSS distribution not only on a cross-section but on the entire volumetric vessel wall even with an arbitrary 3D curvature. As a result, the plot of shear force vectors with the three-directional components provides a facile view of the magnitude and direction of the vector acting on an arbitrary shape of the vessel wall, and enriches clinical information (Bieging et al., 2011; Boussel et al., 2009; Cibis et al., 2016; Guzzardi et al., 2015; Isoda et al., 2010; Naito et al., 2012; Potters et al., 2015; van Ooij et al., 2015, 2016).

Although the estimation of WSS has advanced to a 3D arbitrary shape of vessel and has been applied to diverse clinical studies, few have focused on the validation or accuracy of WSS estimated using 4D flow MRI data, to the best of our knowledge. In fact, it is difficult to discover descriptions about the accuracy of estimated WSS in most of the aforementioned 4D flow MRI studies. This is problematic because it is well known that the spatial resolution of 4D flow MRI is low and consequently, the accuracy of a differential quantity, WSS, is hard to be reliable (Yang et al., 2018). Under a given measurement condition of 4D flow MRI, unfortunately, the improvement of spatial resolution is limited predominantly by the signal-to-noise ratio (SNR) of an MR scanner and the total scan time. Therefore, it is essential to understand how the spatial resolution affects the accuracy of WSS estimation. A couple of recent studies insisted that increasing a relative spatial resolution, which was defined by the number of voxels across the diameter of a lumen, resulted in an improved WSS accuracy (Petersson et al., 2012; Potters et al., 2015). In order to apply WSS information in clinical studies, however, an assessment method to evaluate the accuracy of WSS estimation should be investigated extensively. In other word, it is desirable to suggest a facile method of assessing the WSS estimation accuracy without knowing the flow details like a velocity gradient near wall.

This paper addresses a novel and facile criterion to assess the accuracy of WSS estimation with a given data set of 4D flow MRI. For accurate and inclusive studies, we measured 4D velocities in three circular tubing flow with a diameter of 40, 8, and 2 mm. The 40 mm tubing flow was measured by 3 Tesla (T) human MR scanner with a knee coil and spatial resolution of 0.5 mm. The 8 and 2 mm tubing flows were both measured by 4.7 T MR scanner, but the scans were performed with a conventional birdcage coil (8 mm tubing) and a custom-made solenoid coil (2 mm tubing), respectively. The spatial resolution was varied from 0.2, 0.4 or 0.8 mm for the 8 mm tubing flow, but was fixed at 0.090 mm for 2 mm tubing flow. In addition, five flow rates were considered. Then, we determined WSS for each MR data set using two different methods to estimate a near-wall velocity gradient: the use of a linear velocity profile (LP) vs quadratic velocity profile (QP) assumption. In this study, we also examined the accuracy of velocity measurements and WSS evaluations against the theoretical values provided by the Hagen–Poiseuille equation, and finally proposed the novel and facile criterion, called Reynolds resolution, with which the accuracy of WSS estimation is readily assessed for a given MR measurement condition.

2. Materials and methods

2.1. Experimental setup

Three types of circular tubings were prepared as flow phantoms. Of these, two were acrylic tubings with inner diameters of 40 mm and 8 mm, and one was a Teflon tubing with an inner diameter of 2 mm. Fig. 1 shows the schematic of a closed-loop flow circuit for the 40 mm tubing flow measurements using a 3 T MR machine (Achieva 3 T, Philips, Netherlands). It consists of the tubing, a reservoir, a centrifugal pump (PH-250W-B, Hanil Electric, South Korea), and a turbine flow meter (SPX050, Seametrics, USA) to monitor the flow rate. A 4.7 T MR machine (Biospec 47/40, Bruker, USA) was used for the 8 mm tubing flow measurements, and a fluid flow generated using a micro-gear pump (GJ-N21.JF1S.SE, Micropump, USA) was monitored using a turbine flow meter (IR-Opflow 1, Tecflow International, Netherlands). A similar flow circuit was constructed for the 2 mm tubing flow, but it consisted of a syringe pump (PHD-2000, Harvard Apparatus, USA) without a flow meter because the pump itself could regulate the flow rate. A sufficiently long entrance section of tubing was secured upstream of the measurement section to ensure a fully-developed laminar flow without the entrance effects. All the components of the flow circuit, except the pumps, were made of non-magnetic material to avoid any magnetic field distortion. The pumps were placed far from the MR machine. Both the MR machines were located at Korea Basic Science Institute.

Details of the flow conditions are listed in Table 1. A small amount of copper sulfate was added to deionized water to improve the SNR and shorten the T_1 value of water (Lee et al., 2017). An optimal concentration of the copper sulfate was determined for the two MR machines by measuring the SNR of a static fluid with various concentrations. The flow temperature was monitored and maintained at the room temperature value (25 °C) during the measurements.

Table 2 presents detailed descriptions and sequence settings of the 4D flow MRI measurements. A custom-made solenoid RF coil (Yang et al., 2018) was utilized for the 2 mm tubing flow measurements to improve SNR and achieve a higher spatial resolution (Badilita et al., 2010). The spatial resolutions were set to 0.50, 0.20, and 0.090 mm isotropically, resulting in 80, 40, and 22 voxels across the diameter for the 40, 8, and 2 mm inner diameter tubings, respectively. The SNR of each tubing data was defined by the ratio of MR signal in the center region of tubing to the standard deviation of MR signal out of the tubing area (Bock et al., 2010). In

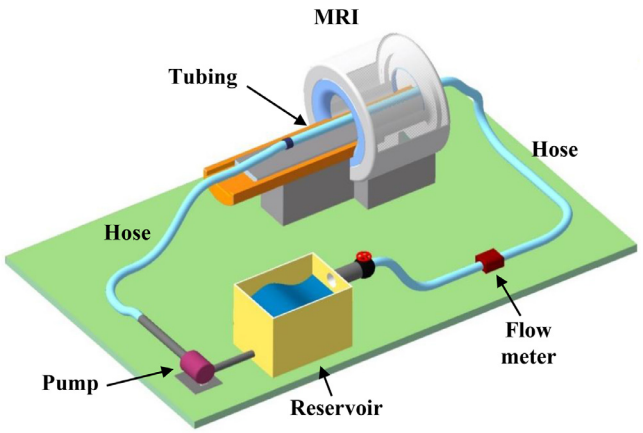

Fig. 1. Schematic of a closed-loop flow circuit. The components may vary depending on a flow characteristic to be measured.

Table 1
Details of different flow conditions. Copper sulfate was added to the deionized water to improve the signal-to-noise ratio of 4D flow MRI measurement results.

Tubing material	Acrylic	Acrylic	Teflon
Specified diameter (mm)	40	8.0	2.0
Measured diameter (mm)	39.8	7.9	2.0
Reynolds number	610	720	100
Flow rate (mL/min)	1150	270	9.50
Working fluid	$CuSO_4$ aqueous solution (40 mM)	$CuSO_4$ aqueous solution (1.0 mM)	$CuSO_4$ aqueous solution (1.0 mM)
Fluid density (kg/m^3)	1000	1000	1000
Fluid viscosity (cP)	1.00	1.00	1.00

Table 2
Detailed descriptions and sequence settings of the 4D flow MRI measurements. The RO, PE, and SE represent read-out, phase-encoding, and slice-encoding, respectively. The FH indicates foot-to-head direction. The definition of Reynolds resolution is presented in Section 2.3.

	40 mm tubing	8 mm tubing	2 mm tubing
MRI machine	Philips 3 T Achieva	Bruker BioSpec 47/40	Bruker BioSpec 47/40
Pulse sequence	QFlow	FLOWMAP	FLOWMAP
Scan mode	3D	3D	3D
RF coil	8-channel knee-coil	Birdcage coil	Custom-made solenoid coil
Spatial resolution (mm)	0.5 (all direction)	0.2 (all direction)	0.090 (all direction)
Field-of-view (mm) (RO, PE, SE)	(128, 64, 64)	(25.6, 12.8, 12.8)	(5.75, 5.75, 11.5)
Acquisition matrix (RO, PE, SE)	(256, 128, 128)	(128, 64, 64)	(64, 64, 128)
Read-out direction	FH	FH	FH
Slice orientation	Coronal	Sagittal	Sagittal
Flip angle (°)	50	15	30
TR / TE (ms)	23 / 14	25 / 4	22/3.8
Encoding velocity (cm/s)	4, 1, 1 (RO, PE, SE)	20 (all direction)	11 (all direction)
Scan time	37 min 30 s	6 min 50 s	12 min 1 s
Signal-to-noise ratio	257.8	109.1	137.6
Reynolds resolution	0.0779	0.367	0.0718

Table 3
Conditions of additional 4D flow MRI experiments for the 8 mm tubing.

	$\Delta x = 0.4$ mm		$\Delta x = 0.8$ mm	
	SNR	Reynolds resolution	SNR	Reynolds resolution
V_{enc} = 10 cm/s(Flow rate: 135 mL/min)	178.9	0.224	293.8	0.272
V_{enc} = 20 cm/s(Flow rate: 270 mL/min)	177.5	0.451	294.3	0.544
V_{enc} = 30 cm/s(Flow rate: 405 mL/min)	178.1	0.674	293.6	0.817
V_{enc} = 40 cm/s(Flow rate: 540 mL/min)	175.3	0.913	290.9	1.100

addition, eight additional experiment sets were performed for the 8 mm tubing to ensure diverse cases, as listed in Table 3.

Finally, to eliminate the artifacts caused by eddy current or system drift, the velocity vectors were obtained by subtracting the flow-off phase data from the flow-on phase data (Elkins and Alley, 2007; Elkins et al., 2003; Lee et al., 2017). Each flow-on and off data set was measured twice and averaged. The data were processed and analyzed with in-house codes built with MATLAB (R2017a, Mathworks, USA).

2.2. Calculation of near-wall velocity gradient

Near-wall velocity gradients should be calculated to evaluate the WSS as shown in Eq. (A.3). The calculation of a near-wall velocity gradient follows two steps: (1) determining the wall boundary with the no-slip condition and (2) taking a derivative of velocity profile constituted with the velocity data adjacent to the wall. In the first step, an optimal threshold magnitude that best divides the flow region and non-flow region is carefully chosen. Specifically, we draw a closed loop connecting the voxels of the threshold value on each tubing slice perpendicular to the flow direction, and compare the loop area with the theoretical tubing area to determine an error in the area. Next, an optimal threshold that minimizes the cross-sectional area error is looked for iteratively. The optimal threshold value is allowed to vary along the streamwise direction due to the inhomogeneity of the applied magnetic field. Therefore, we cut off both ends of the field-of-view (FOV) in the flow direction so that the optimal thresholds in the FOV vary less than 5%. Finally, a 3D isosurface of the averaged optimal threshold value is generated. The isosurface consists of triangular cells (smaller than a voxel) referred to as facets. The centroid of each facet and a unit vector normal to the facet plane are determined by using the coordinates of vertices of the facet. In the present study, the number of facets was approximately 56,000, 26,100, and 13,800 for the 40, 8, and 2 mm tubings, respectively.

In the second step, to obtain the near-wall velocity gradients, two cases were undertaken with different combinations of the velocity profile assumption (linear vs. quadratic). Fig. 2 depicts each case in detail. In both cases, the velocity is considered to be assigned to the center of the voxel. The solid voxel represents a voxel occupied by the solid wall only, and the fluid voxel is filled with the fluid only. Conversely, the boundary voxel is a voxel where the wall boundary is located and thus is occupied by both solid and fluid. The velocity of the boundary voxel is excluded from the velocity profile due to its low SNR (Ha et al., 2016b). The no-slip condition is applied to the center of the wall boundary voxel. Note that the velocity gradient at the wall boundary is a tensor assigned to the center of each boundary voxel. It should be mapped onto the centroid of the facet on the isosurface generated during the segmentation process. Thus, we used an inverse distance weighing method to interpolate the velocity gradient for each facet centroid

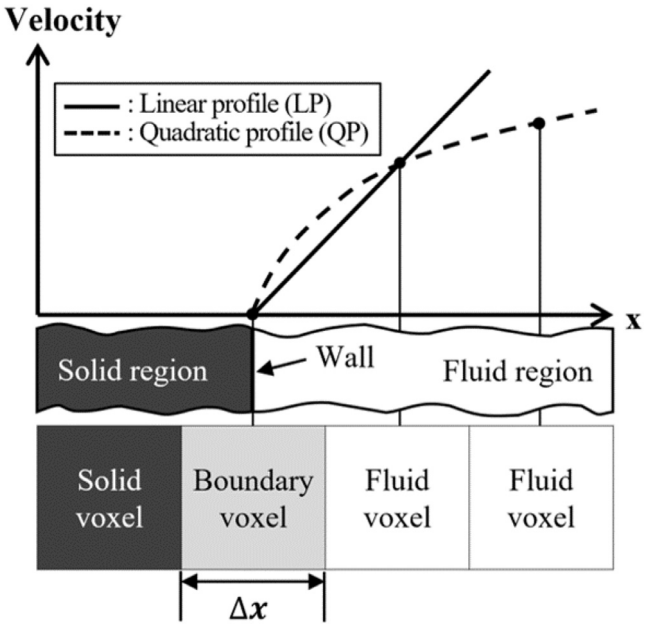

Fig. 2. Two cases for the near-wall velocity gradient calculation, which are differed by the assumption of the near-wall velocity profile (linear vs quadratic). In both cases, the velocity is considered to be given at the center of the voxel. The no-slip condition is applied to the center of a boundary voxel.

using the velocity gradients of the boundary voxels surrounding the facet.

2.3. Criteria to assess the accuracy of WSS estimation

In fluid mechanics, it is well known that the accuracy of velocity measurements depends on two factors: geometric factor and kinematic factor. The former can be represented by the ratio of spatial resolution to characteristic length scale and the latter by the ratio of velocity uncertainty to velocity scale. In 4D flow MRI, the candidates for two factors are the ratio of voxel size to tubing size (i.e., diameter) and the ratio of standard deviation of noise in velocity measurement to the maximum velocity in the tubing. When considering the accuracy of WSS, more importantly, an additional factor should be considered as a dynamic factor. This could be the ratio of WSS to dynamic pressure, which is also called skin friction coefficient in fluid mechanics. Note that the skin friction coefficient is closely related to Reynolds number (Re) that is defined as $Re = \frac{V_{max}D}{\nu}$ for a circular tubing flow, where V_{max} is the maximum velocity of the circular tubing flow, D is the diameter, and ν is the kinematic viscosity of the fluid (i.e., the ratio of the dynamic viscosity to density) (White, 2006).

By considering that the estimation accuracy of the near-wall velocity gradient or WSS with 4D flow MRI measurements is closely related to the three factors and that it should improve with decreasing the three factors, a non-dimensional index can be defined as follows.

$$\frac{\Delta x}{D} \cdot \frac{V_{noise,std}}{V_{max}} \cdot Re \tag{1}$$

where Δx is the voxel size and $V_{noise,\ std}$ is the standard deviation of noise in velocity measurements of 4D flow MRI. By using the definition of Re, Eq. (1) is rearranged as follows.

$$\frac{\Delta x \cdot V_{noise,std}}{\nu} = \text{“}Reynolds\ resolution\text{”} \tag{2}$$

This non-dimensional index is named as “*Reynolds resolution*” because it resembles the definition of Re and consists of terms related to the length scale and velocity scale like Δx and $V_{noise,\ std}$. It is reported that $V_{noise,\ std}$ is proportional to the encoding velocity (V_{enc}) divided by SNR of obtained MR data (Ha et al., 2016b; Pelc et al., 1991). Therefore, Reynolds resolution is also expressed as below.

$$\frac{\Delta x \cdot V_{enc}}{\nu \cdot SNR} \tag{3}$$

Note that the value of Reynolds resolution reduces with decreasing the voxel size or increasing SNR, implying that the WSS accuracy improves.

3. Results

3.1. Evaluation of velocity measurements

The accuracy of velocity measurements was evaluated with the flow rate, an integral parameter, prior to describing differential parameters like the near-wall velocity gradient or WSS. Fig. 3 shows the velocity profile averaged over cross-sections in the field-of-view for each tubing. As seen in the figure, the profiles represent a paraboloid, indicating that the flows are a fully-developed, laminar, circular tubing flow. For a quantitative inspection, the average velocity profiles were plotted along with a theoretical profile obtained with the Hagen–Poiseuille equation (White, 2011). The theoretical profile is along with the experimental data for all the cases as shown in Fig. 3. In addition, the flow rate was computed by integrating the average profile over the cross-section and was compared with the value obtained using the flow meter or regulated by the syringe pump. The results for all the three tubings showed an excellent agreement amongst them; the errors in the average flow rate were below 2.0% for all the three cases.

3.2. Streamwise WSS distribution: qualitative results

The distribution of WSS in the streamwise direction is compared for the three tubing flows as shown in Fig. 4 with theoretical WSS values obtained by using Eq. (A.4). The theoretical values were 3.10, 93.0, and 202 mPa for 40, 8, and 2 mm tubing flows, respectively, considering the measured tubing diameter in Table 2. For a fully-developed, pressure-driven, laminar, circular tubing flow, a uniform distribution of the streamwise WSS is expected (see Eq. (A.4)). There are local high WSS spots on the surface of the 40 mm tubing which might have been caused by small bubbles.

3.3. Streamwise WSS distribution: quantitative results

For quantitative analysis, the streamwise WSS of all the facets were collected and compared with the theoretical WSS. Prior to the analysis, we filtered out outliers in the WSS values. The outliers correspond to erroneous local high/low WSS spots witnessed in Fig. 4 and are caused by roughness or tiny air bubbles of the tubing surface and locally inhomogeneous magnetic field. The outliers were defined as data points out of a range of the two standard deviations from the average of WSS distribution; this filtering process was repeated twice. The number of outliers was approximately 4500 (8%) for the 40 mm tubing, 2000 (8%) for the 8 mm tubing, and 1300 (9%) for the 2 mm tubing. Fig. 5 shows the boxplots of streamwise WSS distribution. The blue box represents the WSS between the first and the third quartile of the distribution and the red line in the box indicates the median. Black dotted lines attached to both the ends of the box display a range 1.5 times that of the box. The theoretical WSS calculated by using Eq. (A.4) is indicated by the thick black line. The LP method showed narrower WSS distribution compared to the QP method. Additionally, the median of the distribution by the LP method was

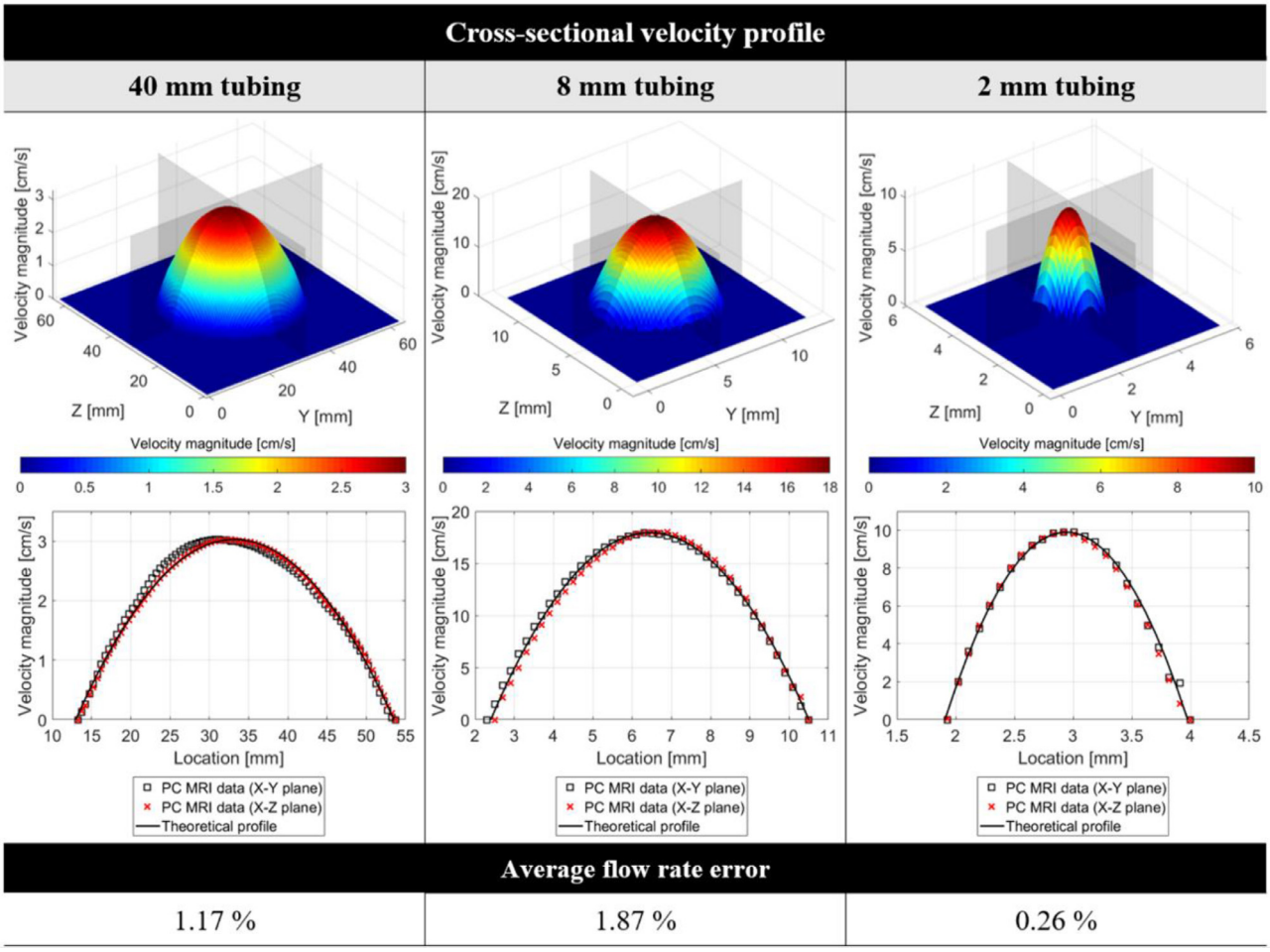

Fig. 3. Cross-sectional velocity profile and flow rate error of each flow. The contour plots represent an average of velocity profile along the streamwise direction. The parabolic profiles are compared at the cross-section of each tubing.

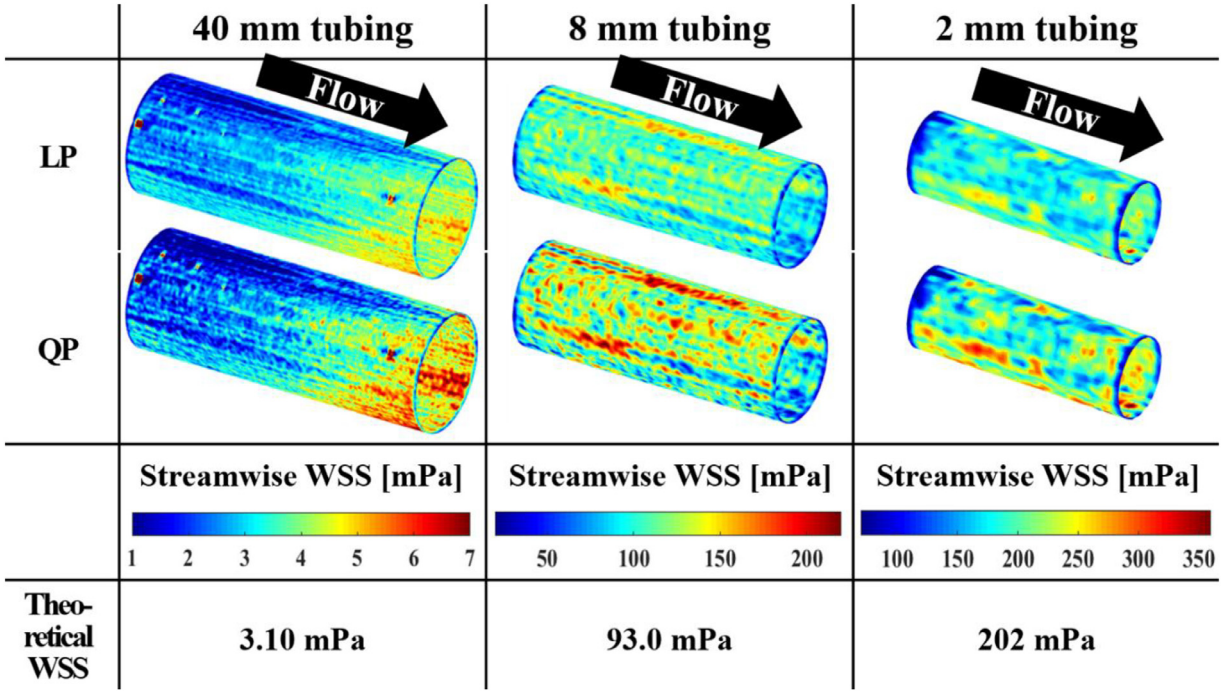

Fig. 4. Distribution of the streamwise WSS on the circular tubing surface. The theoretical WSS values were obtained by using Eq. (A.4).

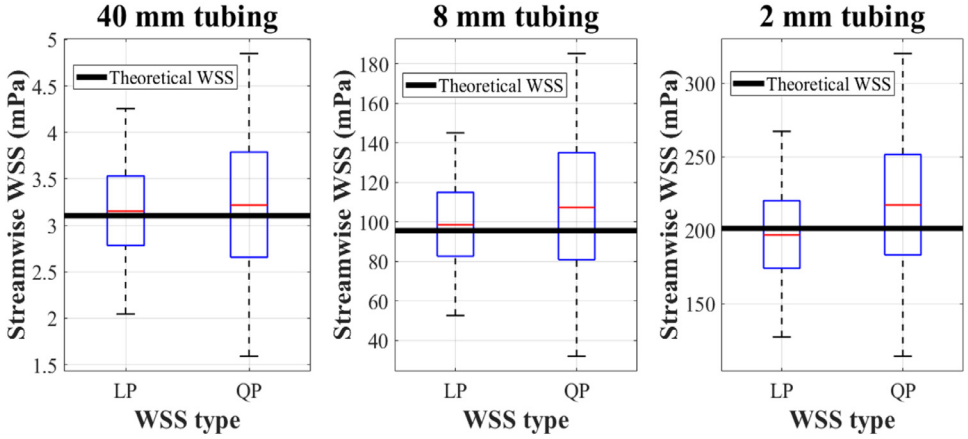

Fig. 5. Boxplot of the streamwise WSS. The blue box represents the WSS between the first and third quartiles of the distribution while the red line inside the box represents the median. Black dotted lines attached to both ends of the box indicate a range 1.5 times the box length. The theoretical WSS values are indicated by the thick black lines. (For interpretation of the references to colour in this figure legend, the reader is referred to the web version of this article.)

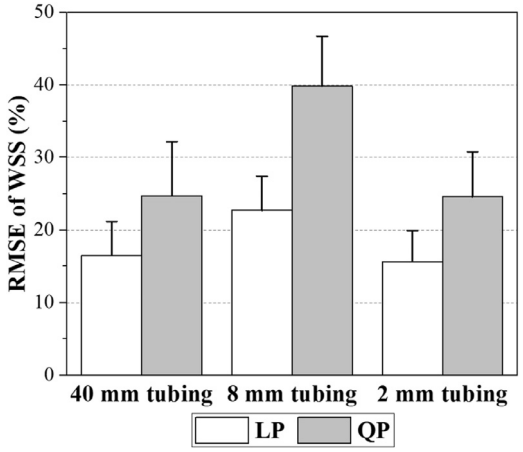

Fig. 6. Root-mean-square error (RMSE) of streamwise WSS. The error was calculated relative to the theoretical WSS. The error bar was calculated by uncertainty analysis considering the uncertainties of velocity measurements and wall position determination.

closer to the theoretical WSS value compared with the QP method. According to the Mann-Whitney *U* test, all the data sets were different from one another in terms of their median at 1% significance level.

Another quantitative analysis was performed by comparing the streamwise WSS on each facet to the theoretical WSS. Fig. 6 shows the root-mean-square error (RMSE) of the streamwise WSS distribution. The RMSE was defined to be a root-mean-square value of relative WSS errors against the theoretical WSS on each facet. Note that the assumption of an LP near the wall resulted in a smaller error than the QP for all the three tubing flows, as can be speculated from Fig. 5. The error bars indicate the two major uncertainties in the WSS estimation. One is a velocity uncertainty calculated by utilizing the encoding velocity and the SNR of 4D flow MRI data (Ha et al., 2016b; Pelc et al., 1991). The other is the uncertainty in determining the wall position in a boundary voxel.

Finally, the errors of flow rate and WSS for the eight additional experiments of 8 mm tubing are listed in Table 4. As described in Section 3.1., the flow rate error was calculated by comparing the averaged flow rate over the cross-section with the value obtained by the flow meter. The flow rate error ranged within ±3.0% and the RMSE of WSS was found over 20% for all cases.

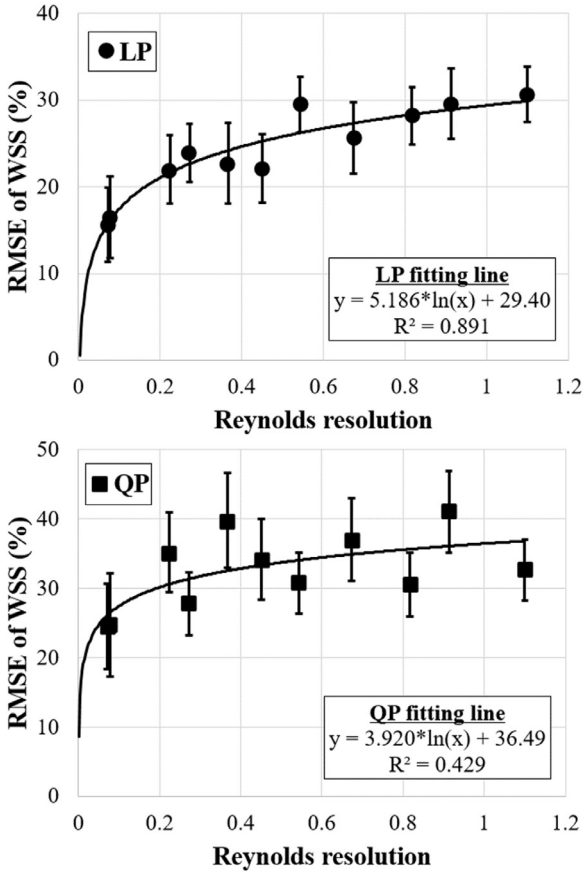

Fig. 7. Relationship between the Reynolds resolution and the RMSE of WSS. The solid line represents a logarithmic fitting line.

3.4. Relation between the error of WSS and Reynolds resolution

The feasibility of assessing the accuracy of WSS with the Reynolds resolution was examined by relating Reynolds resolution to the RMSE of WSS. Fig. 7 depicts the RMSE variation with respect to Reynolds resolution. The solid line represents a logarithmic fitting line. We chose the logarithmic fitting because the WSS error should become zero as a voxel size approaches zero and because it should be asymptotic at a large Reynolds resolution. For the LP

Table 4
Errors in flow rate and WSS of additional experiments for the 8 mm tubing.

	$\Delta x = 0.4$ mm			$\Delta x = 0.8$ mm		
	Flow rate error (%)	RMSE of WSS (%)		Flow rate error (%)	RMSE of WSS (%)	
		LP	QP		LP	QP
$V_{enc} = 10$ cm/s	−0.43	22.0	35.2	2.62	23.9	27.8
$V_{enc} = 20$ cm/s	1.15	22.1	34.2	2.84	29.5	30.8
$V_{enc} = 30$ cm/s	0.36	25.6	37.0	0.69	28.2	30.6
$V_{enc} = 40$ cm/s	−1.26	29.6	41.0	2.10	30.6	32.6

and QP methods, each relation is given as

$$Error\ for\ LP\ (\%) = 5.186 * \ln\left(\frac{\Delta x \cdot V_{noise,std}}{\nu}\right) + 29.40 \quad (4)$$

$$Error\ for\ QP\ (\%) = 3.920 * \ln\left(\frac{\Delta x \cdot V_{noise,std}}{\nu}\right) + 36.49 \quad (5)$$

The R^2 value of the fitting line is 0.891 for the LP method and 0.429 for the QP method. It shows that the RMSE increases with increasing the value of Reynolds resolution.

4. Discussion

The WSS is known to play an important role in CVD, but is yet to be frequently utilized in clinical practice. This is mainly because the WSS estimation lacks validity and reliability. We have measured three, fully-developed, laminar, circular tubing flows of different diameters and flow rates using 4D flow MRI with different spatial resolutions and MR sequences in order to assess the WSS accuracy with the data from extensive measurements. To obtain the near-wall velocity gradient for determining WSS, two methods were adopted with the assumption of linear and quadratic velocity profiles. More importantly, we proposed a non-dimensional index, called Reynolds resolution, which is in logarithmic relation with the error in WSS estimation, to be able to readily evaluate the WSS estimation using 4D flow MRI.

4.1. Accuracy in velocity measurements and WSS calculation

It is confirmed that 4D flow MRI results were estimated accurately in terms of either flow rate or velocity profile as shown in Fig. 3. Despite using different MR scanners, MR sequences, RF coils, tubing geometries and flow rates, all the velocity measurements were quite accurate. However, this does not guarantee the accuracy of the near-wall velocity gradient or WSS. It is important to properly select the calculation method for a given set of MR data.

The LP and QP methods use a forward or backward difference scheme to obtain a near-wall velocity gradient applying the no-slip condition to the center of wall boundary voxel. The LP method shows more agreement with the theoretical WSS in its median value compared to the QP method (Fig. 5). Interestingly, the median of WSS distribution estimated by using QP method is overestimated in all the tubings. An earlier work also reported an overestimation with a quadratic velocity profile as in the present results, but an underestimation with a linear velocity profile (Petersson et al., 2012).

4.2. Definition and feasibility of Reynolds resolution

The definition of Reynolds resolution (Eq. (2)) is suggested in the course of considering that the accuracy of WSS estimation by 4D flow MRI is affected by both the MR settings and flow conditions. The former includes the spatial resolution and noise in velocity measurements, representing geometric and kinematic factors, respectively. The latter, which corresponds to a dynamic factor, can be represented by *Re* because the WSS scale (or magnitude) depends on it. In fact, the results of RMSE of WSS shown in Fig. 6 indicate that the WSS error seems to be independent of the tube size and spatial resolution (Table 2). For example, the 8 mm tubing resulted in the largest RMSE with both the LP and QP methods although it is measured with a better spatial resolution than the 40 mm tubing and has a larger diameter than the 2 mm tubing. In addition, the flow of 8 mm tubing had a lower flow rate than that of 40 mm tubing but the highest *Re*. This inspection led to a hypothesis that the error would depend on *Re* in addition to the geometric and kinematic factors.

It is reasonable to believe that a better spatial resolution (smaller voxel size) would lead to a more accurate WSS estimation for a given condition of measurement and flow because it would capture a steep change in velocity near the wall. Additionally, when reducing the standard deviation of velocity noise depending on the encoding velocity and the SNR (Ha et al., 2016b; Pelc et al., 1991), the uncertainty of velocity measurements would reduce and the accuracy of WSS estimation would improve. Finally, it has been reported that a WSS estimation becomes less accurate as the theoretical WSS (or WSS scale) increases (Petersson et al., 2012). Note that the WSS scale is represented by *Re* (White, 2011). Therefore, it is appropriate to define the Reynolds resolution as a multiplication of the aforementioned three factors.

Note that the Reynolds resolution depends on the kinematic viscosity (ratio of fluid dynamic viscosity to density) as well. The kinematic viscosity is related to the momentum transfer rate and is often called momentum diffusivity (White, 2011). The momentum transfer between fluid elements occurs actively with a large kinematic viscosity and a velocity gradient is likely to be relaxed quickly. Hence, this term should be included in the Reynolds resolution as it represents how rapidly a flow can adjust itself when disturbed by a flow pulsation or abrupt change in flow geometry like a stenosis.

In order to examine the feasibility of the Reynolds resolution, the RMSE of WSS estimated by 4D flow MRI (Fig. 6) were accurately evaluated against the theoretical value *a priori*, which is a reason to perform in vitro measurements of 4D flow MRI for a circular tubing flow. The comparison of the error and Reynolds resolution revealed a logarithmic relation between them (Fig. 7). The relation is quite clear in the case of LP ($R^2 = 0.891$), but the results of QP method are scattered around the fitting line ($R^2 = 0.429$) as compared to the LP method. This may be attributed to the fact that the QP method utilizes two velocity data while the LP method uses only one (Fig. 2). Since each velocity is subject to an uncertainty, using more velocity points would result in a larger uncertainty in a WSS estimation. This is evidenced by the fact that the error bar of the QP method is larger than that of LP method. Nevertheless, these results are encouraging because one can readily evaluate the accuracy of WSS estimation with near-wall velocities measured by 4D flow MRI with a simple algebraic calculation of the Reynolds resolution to the first order approximation. It is important to note that the concept of assessing the WSS accuracy with Reynolds resolution would be valid even if a flow is subject

to a pulsation because their relation was determined based on the near-wall velocity gradient defining the WSS.

Finally, it should be noted that the accuracy of WSS estimation depends not only on the three factors considered in the definition of Reynolds resolution but also on the accuracy of the wall boundary location. This depends on an absolute spatial resolution rather than the relative resolution. We assumed that the wall boundary is fixed at the center of the boundary voxel (Fig. 2). As per earlier studies, considering the partial volume effects in 4D flow MRI data may help improve the accuracy in the wall position estimation with a high spatial resolution (Potters et al., 2015). Thus, a comparison of the WSS accuracy via Reynolds resolution between different 4D flow MRI measurements should be conducted under the condition of a similar accuracy in wall position determination.

4.3. Limitations

One of the limitations using Reynolds resolution for assessing WSS accuracy is that the relation between them has been suggested with the MR data measured for the fully-developed, laminar, circular tubing flows. In fact, in vivo studies are likely to be a complex flow such as a transient flow, pulsatile flow, and turbulent flow. The results of this study may or may not be altered for such a complex flow although the Reynolds resolution was defined to be applicable to such a flow. Therefore, it is necessary to investigate whether or not the concept of Reynolds resolution is valid to in vivo studies. In addition, the effects of other 4D flow MRI conditions like the slice orientation, flip angle, repetition time, and echo time need to be further examined on the validity of Reynolds resolution. Finally, the relationship between the Reynolds resolution and the WSS accuracy was discovered with only 4D flow MRI experiment data sets. Data from numerical simulation results such as in the work by Petersson et al. (2012) would enrich the relationship with more diverse cases.

5. Conclusions

This paper addresses a novel and facile criterion called Reynolds resolution to assess the WSS accuracy estimated by 4D flow MRI. A simple algebraic calculation with the voxel size, standard deviation of noise in velocity measurements, and kinematic viscosity of fluid results in the WSS error estimation to the first approximation. A logarithmic relation has been established between the Reynolds resolution and WSS error after extensive studies on MR data obtained using different circular tubing flows of different tubing diameter, different MR scanners, different spatial resolutions, etc. We believe that the present results will have impact on the hemodynamic studies on CVD because one can readily estimate and report an estimated WSS error using the Reynolds resolution without having a theoretical WSS.

Acknowledgments

This work was supported by the National Research Foundation of Korea (NRF) grant funded by the Korea government (No. 2016R1A2B3009541 and 2012R1A6A1029029).

Conflict of interest

The authors declare no conflict of interest.

Appendix A. WSS calculation

A WSS indicates the tangential component of a force exerted on a unit area of the wall by a fluid flow. The force exerted on the wall can be described as,

$$\vec{F} = \mu(2\dot{\varepsilon}\cdot\vec{n}) \tag{A.1}$$

where $\vec{F}$ is the force vector, μ is the dynamic viscosity of the fluid, $\dot{\varepsilon}$ is the strain rate tensor and $\vec{n}$ is the unit normal vector to the surface of the wall (i.e., flow boundary). Note that Eq. (A.1) holds for an incompressible and Newtonian fluid. Then, the shear force is computed by extracting the tangential component of the force which can be determined using the equation below.

$$\vec{F_s} = \vec{F} - \left(\vec{F}\cdot\vec{n}\right)\vec{n} \tag{A.2}$$

where $\vec{F_s}$ is the shear force vector. The WSS is defined by dividing it with the unit area of the wall. The strain rate tensor in Eq. (A.1) is defined by the gradient of the velocity field and it is expressed as,

$$\dot{\varepsilon} = \begin{bmatrix} \frac{\partial u}{\partial x} & \frac{1}{2}\left(\frac{\partial u}{\partial y}+\frac{\partial v}{\partial x}\right) & \frac{1}{2}\left(\frac{\partial u}{\partial z}+\frac{\partial w}{\partial x}\right) \\ \frac{1}{2}\left(\frac{\partial v}{\partial x}+\frac{\partial u}{\partial y}\right) & \frac{\partial v}{\partial y} & \frac{1}{2}\left(\frac{\partial v}{\partial z}+\frac{\partial w}{\partial y}\right) \\ \frac{1}{2}\left(\frac{\partial w}{\partial x}+\frac{\partial u}{\partial z}\right) & \frac{1}{2}\left(\frac{\partial w}{\partial y}+\frac{\partial v}{\partial z}\right) & \frac{\partial w}{\partial z} \end{bmatrix} \tag{A.3}$$

where u, v, and w correspond to the components of a velocity vector along x, y, and z direction, respectively.

For a fully-developed, pressure-driven laminar circular tubing flow, the Hagen–Poiseuille equation gives a theoretical WSS value (τ_t) as follows.

$$\tau_t = \frac{4\mu Q}{AR} \tag{A.4}$$

where Q is the flow rate, A is the cross-sectional area, and R is the tubing radius. All of the parameters in Eq. (A.4), except for the dynamic viscosity, were derived from the 4D flow MRI results. The theoretical WSS value is served as the reference value for the accuracy evaluation of WSS estimated from different cases of near-wall velocity gradient calculations.

References

Badilita, V., Kratt, K., Baxan, N., Mohmmadzadeh, M., Burger, T., Weber, H., Elverfeldt, D.V., Hennig, J., Korvink, J.G., Wallrabe, U., 2010. On-chip three dimensional microcoils for MRI at the microscale. Lab Chip 10 (11), 1387–1390.

Bieging, E.T., Frydrychowicz, A., Wentland, A., Landgraf, B.R., Johnson, K.M., Wieben, O., François, C.J., 2011. In vivo three-dimensional MR wall shear stress estimation in ascending aortic dilatation. J. Magn. Reson. Imaging 33 (3), 589–597.

Bock, J., Frydrychowicz, A., Stalder, A.F., Bley, T.A., Burkhardt, H., Hennig, J., Markl, M., 2010. 4D phase contrast MRI at 3 T: effect of standard and blood-pool contrast agents on SNR, PC-MRA, and blood flow visualization. Magn. Reson. Med. 63 (2), 330–338.

Boussel, L., Rayz, V., Martin, A., Acevedo-Bolton, G., Lawton, M.T., Higashida, R., Smith, W.S., Young, W.L., Saloner, D., 2009. Phase-contrast magnetic resonance imaging measurements in intracranial aneurysms in vivo of flow patterns, velocity fields, and wall shear stress: comparison with computational fluid dynamics. Magn. Reson. Med. 61 (2), 409–417.

Bürk, J., Blanke, P., Stankovic, Z., Barker, A., Russe, M., Geiger, J., Frydrychowicz, A., Langer, M., Markl, M., 2012. Evaluation of 3D blood flow patterns and wall shear stress in the normal and dilated thoracic aorta using flow-sensitive 4D CMR. J. Cardiovasc. Magn. Reson. 14 (1), 84.

Calkoen, E.E., Roest, A.A., Kroft, L.J., van der Geest, R.J., Jongbloed, M.R., van den Boogaard, P.J., Blom, N.A., Hazekamp, M.G., de Roos, A., Westenberg, J.J., 2015. Characterization and improved quantification of left ventricular inflow using streamline visualization with 4DFlow MRI in healthy controls and patients after atrioventricular septal defect correction. J. Magn. Reson. Imaging 41 (6), 1512–1520.

Cebral, J.R., Putman, C.M., Alley, M.T., Hope, T., Bammer, R., Calamante, F., 2009. Hemodynamics in normal cerebral arteries: qualitative comparison of 4D phase-contrast magnetic resonance and image-based computational fluid dynamics. J. Eng. Math. 64 (4), 367–378.

Cecchi, E., Giglioli, C., Valente, S., Lazzeri, C., Gensini, G.F., Abbate, R., Mannini, L., 2011. Role of hemodynamic shear stress in cardiovascular disease. Atherosclerosis 214 (2), 249–256.

Cibis, M., Potters, W.V., Selwaness, M., Gijsen, F.J., Franco, O.H., Arias Lorza, A.M., de Bruijne, M., Hofman, A., van der Lugt, A., Nederveen, A.J., Wentzel, J.J., 2016. Relation between wall shear stress and carotid artery wall thickening MRI versus CFD. J. Biomech. 49 (5), 735–741.

Donati, F., Figueroa, C.A., Smith, N.P., Lamata, P., Nordsletten, D.A., 2015. Non-invasive pressure difference estimation from PC-MRI using the work-energy equation. Med. Image Anal. 26 (1), 159–172.
Dyverfeldt, P., Bissell, M., Barker, A.J., Bolger, A.F., Carlhall, C.J., Ebbers, T., Francios, C.J., Frydrychowicz, A., Geiger, J., Giese, D., Hope, M.D., Kilner, P.J., Kozerke, S., Myerson, S., Neubauer, S., Wieben, O., Markl, M., 2015. 4D flow cardiovascular magnetic resonance consensus statement. J. Cardiovasc. Magn. Reson. 17, 72.
Dyverfeldt, P., Hope, M.D., Tseng, E.E., Saloner, D., 2013. Magnetic resonance measurement of turbulent kinetic energy for the estimation of irreversible pressure loss in aortic stenosis. JACC Cardiovasc. Imaging 6 (1), 64–71.
Ebbers, T., Wigström, L., Bolger, A.F., Engvall, J., Karlsson, M., 2001. Estimation of relative cardiovascular pressures using time-resolved three-dimensional phase contrast MRI. Magn. Reson. Med. 45 (5), 872–879.
Elkins, C.J., Alley, M.T., 2007. Magnetic resonance velocimetry: applications of magnetic resonance imaging in the measurement of fluid motion. Exp. Fluids 43 (6), 823–858.
Elkins, C.J., Markl, M., Pelc, N., Eaton, J.K., 2003. 4D Magnetic resonance velocimetry for mean velocity measurements in complex turbulent flows. Exp. Fluids 34 (4), 494–503.
Guzzardi, D.G., Barker, A.J., van Ooij, P., Malaisrie, S.C., Puthumana, J.J., Belke, D.D., Mewhort, H.E., Svystonyuk, D.A., Kang, S., Verma, S., Collins, J., Carr, J., Bonow, R.O., Markl, M., Thomas, J.D., McCarthy, P.M., Fedak, P.W., 2015. Valve-related hemodynamics mediate human bicuspid aortopathy: insights from wall shear stress mapping. J. Am. Coll. Cardiol. 66 (8), 892–900.
Ha, H., Hwang, D., Kim, G.B., Kweon, J., Lee, S.J., Baek, J., Kim, Y.H., Kim, N., Yang, D.H., 2016a. Estimation of turbulent kinetic energy using 4D phase-contrast MRI: effect of scan parameters and target vessel size. Magn. Reson. Imaging 34 (6), 715–723.
Ha, H., Kim, G.B., Kweon, J., Kim, Y.H., Kim, N., Yang, D.H., Lee, S.J., 2016b. Multi-VENC acquisition of four-dimensional phase-contrast MRI to improve precision of velocity field measurement. Magn. Reson. Med. 75 (5), 1909–1919.
Harloff, A., Nussbaumer, A., Bauer, S., Stalder, A.F., Frydrychowicz, A., Weiller, C., Hennig, J., Markl, M., 2010. In vivo assessment of wall shear stress in the atherosclerotic aorta using flow-sensitive 4D MRI. Magn. Reson. Med. 63 (6), 1529–1536.
Hope, T.A., Kvitting, J.P., Hope, M.D., Miller, D.C., Markl, M., Herfkens, R.J., 2013. Evaluation of Marfan patients status post valve-sparing aortic root replacement with 4D flow. Magn. Reson. Imaging 31 (9), 1479–1484.
Isoda, H., Ohkura, Y., Kosugi, T., Hirano, M., Takeda, H., Hiramatsu, H., Yamashita, S., Takehara, Y., Alley, M.T., Bammer, R., Pelc, N.J., Namba, H., Sakahara, H., 2010. In vivo hemodynamic analysis of intracranial aneurysms obtained by magnetic resonance fluid dynamics (MRFD) based on time-resolved three-dimensional phase-contrast MRI. Neuroradiology 52 (10), 921–928.
Kochanek, K.D., Murphy, S.L., Xu, J., Tejada-Vera, B., 2016. Deaths: final Data for 2014. Natl. Vital Stat. Rep. 65 (4), 1–122.
Kolipaka, A., Illapani, V.S., Kalra, P., Garcia, J., Mo, X., Markl, M., White, R.D., 2017. Quantification and comparison of 4D-flow MRI-derived wall shear stress and MRE-derived wall stiffness of the abdominal aorta. J. Magn. Reson. Imaging 45 (3), 771–778.
Lee, J., Ko, S., Cho, J.-H., Song, S., 2017. Validation of magnetic resonance velocimetry for mean velocity measurements of turbulent flows in a circular pipe. J. Mech. Sci. Technol. 31 (3), 1275–1282.
Malek, A.M., Alper, S.L., Izumo, S., 1999. Hemodynamic shear stress and its role in atherosclerosis. JAMA 282 (21), 2035–2042.
Markl, M., Brendecke, S.M., Simon, J., Barker, A.J., Weiller, C., Harloff, A., 2013. Co-registration of the distribution of wall shear stress and 140 complex plaques of the aorta. Magn. Reson. Imaging 31 (7), 1156–1162.
Markl, M., Wegent, F., Zech, T., Bauer, S., Strecker, C., Schumacher, M., Weiller, C., Hennig, J., Harloff, A., 2010. In vivo wall shear stress distribution in the carotid artery: effect of bifurcation geometry, internal carotid artery stenosis, and recanalization therapy. Circ. Cardiovasc. Imaging 3 (6), 647–655.
Meierhofer, C., Schneider, E.P., Lyko, C., Hutter, A., Martinoff, S., Markl, M., Hager, A., Hess, J., Stern, H., Fratz, S., 2013. Wall shear stress and flow patterns in the ascending aorta in patients with bicuspid aortic valves differ significantly from tricuspid aortic valves: a prospective study. Eur. Heart J. Cardiovasc. Imaging 14 (8), 797–804.
Montalba, C., Urbina, J., Sotelo, J., Andia, M.E., Tejos, C., Irarrazaval, P., Hurtado, D.E., Valverde, I., Uribe, S., 2018. Variability of 4D flow parameters when subjected to changes in MRI acquisition parameters using a realistic thoracic aortic phantom. Magn. Reson. Med. 79 (4), 1882–1892.
Morbiducci, U., Ponzini, R., Rizzo, G., Cadioli, M., Esposito, A., De Cobelli, F., Del Maschio, A., Montevecchi, F.M., Redaelli, A., 2009. In vivo quantification of helical blood flow in human aorta by time-resolved three-dimensional cine phase contrast magnetic resonance imaging. Ann. Biomed. Eng. 37 (3), 516–531.
Naito, T., Miyachi, S., Matsubara, N., Isoda, H., Izumi, T., Haraguchi, K., Takahashi, I., Ishii, K., Wakabayashi, T., 2012. Magnetic resonance fluid dynamics for intracranial aneurysms—comparison with computed fluid dynamics. Acta Neurochir. 154 (6), 993–1001.
Pantos, I., Patatoukas, G., Efstathopoulos, E.P., Katritsis, D., 2007. In vivo wall shear stress measurements using phase-contrast MRI. Expert Rev. Cardiovasc. Ther. 5 (5), 927–938.
Pelc, N.J., Bernstein, M.A., Shimakawa, A., Glover, G.H., 1991. Encoding strategies for three-direction phase-contrast MR imaging of flow. J. Magn. Reson. Imaging 1 (4), 405–413.
Petersson, S., Dyverfeldt, P., Ebbers, T., 2012. Assessment of the accuracy of MRI wall shear stress estimation using numerical simulations. J. Magn. Reson. Imaging 36 (1), 128–138.
Potters, W.V., van Ooij, P., Marquering, H., vanBavel, E., Nederveen, A.J., 2015. Volumetric arterial wall shear stress calculation based on cine phase contrast MRI. J. Magn. Reson. Imaging 41 (2), 505–516.
Reneman, R.S., Arts, T., Hoeks, A.P., 2006. Wall shear stress–an important determinant of endothelial cell function and structure–in the arterial system in vivo. Discrepancies with theory. J. Vasc. Res. 43 (3), 251–269.
She, H.L., Roest, A.A.W., Calkoen, E.E., van den Boogaard, P.J., van der Geest, R.J., Hazekamp, M.G., de Roos, A., Westenberg, J.J.M., 2017. Comparative evaluation of flow quantification across the atrioventricular valve in patients with functional univentricular heart after fontan's surgery and healthy controls: measurement by 4D flow magnetic resonance imaging and streamline visualization. Congenit. Heart Dis. 12 (1), 40–48.
Sotelo, J., Urbina, J., Valverde, I., Tejos, C., Irarrazaval, P., Andia, M.E., Uribe, S., Hurtado, D.E., 2016. 3D quantification of wall shear stress and oscillatory shear index using a finite-element method in 3D CINE PC-MRI data of the thoracic aorta. IEEE Trans. Med. Imaging 35 (6), 1475–1487.
Strecker, C., Harloff, A., Wallis, W., Markl, M., 2012. Flow-sensitive 4D MRI of the thoracic aorta: comparison of image quality, quantitative flow, and wall parameters at 1.5 T and 3 T. J. Magn. Reson. Imaging 36, 1097–1103.
Tsuji, T., Suzuki, J.-i., Shimamoto, R., Yamazaki, T., Nakajima, T., Nagai, R., Komatsu, S., Ohtomo, K., Toyo-oka, T., Omata, M., 2002. Vector analysis of the wall shear rate at the human aortoiliac bifurcation using cine mr velocity mapping. Am. J. Roentgenol. 178 (4), 995–999.
van Ooij, P., Markl, M., Collins, J.D., Carr, J.C., Rigsby, C., Bonow, R.O., Malaisrie, S.C., McCarthy, P.M., Fedak, P.W.M., Barker, A.J., 2017. Aortic valve stenosis alters expression of regional aortic wall shear stress: new insights from a 4-dimensional flow magnetic resonance imaging study of 571 subjects. J. Am. Heart Assoc. 6 (9), e005959.
van Ooij, P., Potters, W.V., Nederveen, A.J., Allen, B.D., Collins, J., Carr, J., Malaisrie, S.C., Markl, M., Barker, A.J., 2015. A methodology to detect abnormal relative wall shear stress on the full surface of the thoracic aorta using four-dimensional flow MRI. Magn. Reson. Med. 73 (3), 1216–1227.
van Ooij, P., Powell, A.L., Potters, W.V., Carr, J.C., Markl, M., Barker, A.J., 2016. Reproducibility and interobserver variability of systolic blood flow velocity and 3D wall shear stress derived from 4D flow MRI in the healthy aorta. J. Magn. Reson. Imaging 43 (1), 236–248.
Wahle, A., Lopez, J.J., Olszewski, M.E., Vigmostad, S.C., Chandran, K.B., Rossen, J.D., Sonka, M., 2006. Plaque development, vessel curvature, and wall shear stress in coronary arteries assessed by X-ray angiography and intravascular ultrasound. Med. Image Anal. 10 (4), 615–631.
White, F.M., 2006. Viscous Fluid Flow, third ed. McGraw Hill, New York.
White, F.M., 2011. Fluid Mechanics, seventh ed. McGraw Hill, New York.

Further reading

Yang, B., Cho, J.H., Lee, J., Song, S., 2018. Characterization of a custom-made RF coil for a high spatial resolution magnetic resonance velocimetry. J. Mech. Sci. Technol. (in press).